

UC Davis

UC Davis Previously Published Works

Title

A novel tarantula toxin stabilizes the deactivated voltage sensor of bacterial sodium channel

Permalink

<https://escholarship.org/uc/item/24d041kx>

Journal

The FASEB Journal, 31(7)

ISSN

0892-6638

Authors

Tang, Cheng
Zhou, Xi
Nguyen, Phuong Tran
et al.

Publication Date

2017-07-01

DOI

10.1096/fj.201600882r

Peer reviewed

A novel tarantula toxin stabilizes the deactivated voltage sensor of bacterial sodium channel

Cheng Tang,^{*1} Xi Zhou,^{*1} Phuong Tran Nguyen,[†] Yunxiao Zhang,^{*} Zhaotun Hu,^{*} Changxin Zhang,^{*} Vladimir Yarov-Yarovoy,[†] Paul G. DeCaen,[‡] Songping Liang,^{*2} and Zhonghua Liu^{*3}

^{*}The National and Local Joint Engineering Laboratory of Animal Peptide Drug Development, College of Life Sciences, Hunan Normal University, Changsha, China; [†]Department of Physiology and Membrane Biology, University of California Davis, Davis, California, USA; and

[‡]Department of Pharmacology, Feinberg School of Medicine, Northwestern University, Chicago Illinois, USA

ABSTRACT: Voltage-gated sodium channels (Na_vs) are activated by transiting the voltage sensor from the deactivated to the activated state. The crystal structures of several bacterial Na_vs have captured the voltage sensor module (VSM) in an activated state, but structure of the deactivated voltage sensor remains elusive. In this study, we sought to identify peptide toxins stabilizing the deactivated VSM of bacterial Na_vs. We screened fractions from several venoms and characterized a cystine knot toxin called JZTx-27 from the venom of tarantula *Chilobrachys jingzhao* as a high-affinity antagonist of the prokaryotic Na_vs nonselective voltage-gated, *Bacillus alcalophilus* (Ns_vBa) and bacterial sodium channel from *Bacillus halodurans* (NaChBac) (IC₅₀ = 112 nM and 30 nM, respectively). JZTx-27 was more efficacious at weaker depolarizing voltages and significantly slowed the activation but accelerated the deactivation of Ns_vBa, whereas the local anesthetic drug lidocaine was shown to antagonize Ns_vBa without affecting channel gating. Mutation analysis confirmed that JZTx-27 bound to S3-4 linker of Ns_vBa, with F98 being the critical residue in determining toxin affinity. All electrophysiological data and *in silico* analysis suggested that JZTx-27 trapped VSM of Ns_vBa in one of the deactivated states. In mammalian Na_vs, JZTx-27 preferably inhibited the inactivation of Na_v1.5 by targeting the fourth transmembrane domain. To our knowledge, this is the first report of peptide antagonist for prokaryotic Na_vs. More important, we proposed that JZTx-27 stabilized the Ns_vBa VSM in the deactivated state and may be used as a probe to determine the structure of the deactivated VSM of Na_vs.—Tang, C., Zhou, X., Nguyen, P. T., Zhang, Y., Hu, Z., Zhang, C., Yarov-Yarovoy, V. DeCaen, P. G. Liang, S., Liu, Z. A novel tarantula toxin stabilizes the deactivated voltage sensor of bacterial sodium channel. *FASEB J.* 31, 000–000 (2017). www.fasebj.org

KEY WORDS: peptide toxin · deactivated state · Ns_vBa

Mutations in Na_vs cause a variety of diseases of the heart and central and peripheral nervous systems (e.g., long QT syndrome and epilepsy) (1, 2). Many of these mutations are found within the voltage-sensor

modules (VSMs) of Na_vs, which alter the voltage-dependent kinetics of the channel gating (3–5). Understanding structure and function of the voltage sensor of Na_vs will provide insight into the molecular basis of electrical signaling in normal and diseased conditions.

Eukaryotic Na_vs are large proteins with 24 transmembrane segments, making them challenging to study by using crystallographic techniques (6). Several laboratories have crystallized Na_vs from bacteria, which are relatively small and homotetrameric (7–10). Four monomers of bacterial Na_vs assemble to form a channel. Analogous to the 4 domains (I–IV) of eukaryotic Na_vs, each bacterial channel monomer contains a voltage sensor and a pore domain. For prokaryotic Na_vs, the first 4 transmembrane segments (S1–4) form a voltage sensor module (VSM) and the last 2 transmembrane segments (S5 and -6) comprise the pore-forming module. Both eukaryotic and prokaryotic Na_vs are voltage sensitive due to an arrangement of several conserved arginine or lysine residues (called gating charges) located within the S4 segment. During voltage sensor

ABBREVIATIONS: τ_{activation}, activation time constant; τ_{deactivation}, deactivation time constant; ASIC, acid-sensing ion channel; DRG, dorsal root ganglion; ICK, inhibitor cystine knot; I_{Na}, Na⁺ current; NaChBac, bacterial sodium channel from *Bacillus halodurans*; Na_vs, voltage-gated sodium channels; Na_vPZ, sodium channels from *Paracoccus zeaxanthifaciens*; Na_vSP, sodium channels from *Silicibacter pomeroyi*; Ns_vBa, nonselective voltage-gated, *Bacillus alcalophilus*; RP-HPLC, reverse phase-HPLC; VSM, voltage sensor module; WT, wild type

¹ These authors contributed equally to this work.

² Correspondence: The National and Local Joint Engineering Laboratory of Animal Peptide Drug Development, College of Life Sciences, Hunan Normal University, Changsha 410081, Hunan, China. E-mail: liangsp@hunnu.edu.cn

³ Correspondence: The National and Local Joint Engineering Laboratory of Animal Peptide Drug Development, College of Life Sciences, Hunan Normal University, Changsha 410081, Hunan, China. E-mail: liuzh@hunnu.edu.cn

doi: 10.1096/fj.201600882R

This article includes supplemental data. Please visit <http://www.fasebj.org> to obtain this information.

activation, the gating charges move toward the extracellular side in response to membrane depolarization (11).

Prokaryotic Na_vs were thought to be Na⁺-selective (12, 13). Recently, a nonselective member of this family was characterized from *Bacillus alcalophilus* (Ns_vBa: nonselective voltage-gated *B. alcalophilus*) (14). This channel exhibits a unique selectivity filter (sequence: TLDSWGSG) which conducts K⁺ as well as Na⁺ ions, an adaptation that allows *B. alcalophilus* to grow in high-K⁺ conditions (15). Crystal structures from the full-length bacterial channels Na_vAb and Na_vRh exhibit voltage sensors in partially and fully activated states (7, 9). In conjunction with previous work, these structures have provided many mechanistic details of interactions within the voltage sensor that occur during the transition from the partially activated state to the fully activated state. However, the structure of the deactivated voltage sensor has not been solved and needs further investigation.

Several peptide toxins from venomous arachnids and insects stabilize deactivated or activated states of the VSM of ion channels (16–19). These toxins can be exploited by structural biologists to trap voltage sensors in specific states. Several peptide toxins acting on mammalian Na_vs through different mechanisms have been characterized. The α and β scorpion toxins trap domain IV S4 and domain II S4 in the closed and activated conformation, respectively (20, 21). Crystal complexes of the Na_vMs (a prokaryotic Na_v) pore with several brominated drugs depict a common binding site shared by eukaryotic Na_vs (22), but whether a peptide neurotoxin binding site is shared by prokaryotic and eukaryotic Na_vs is unknown. The present study describes the purification and characterization of a novel peptide toxin (JZTx-27) from the venom of the Chinese tarantula, *Chilobrachys jingzhao*. JZTx-27 binds to the extracellular S3-4 loop of the voltage sensor and prevents activation of Ns_vBa by stabilizing the deactivated state. JZTx-27 also acts on the mammalian Na_v1 superfamily with a variable potency. However, JZTx-27 appears to bind to mammalian Na_vs and prevents the inactivation process. This novel tarantula toxin can be used as a molecular probe to further investigate the structural determinants of the deactivated state of sodium channel voltage sensors.

MATERIALS AND METHODS

Venom and toxin purification

The venom of *Chilobrachys jingzhao* was collected by electrical stimulation. The crude venom was lyophilized and preserved at –80°C before use. The crude venom was dissolved in double-distilled H₂O to a final concentration of 5 mg/mL and subjected to semipreparative reverse phase (RP)-HPLC purification (C18 column, 10 μm, 10 × 250 mm; Welch Materials, Inc., Shanghai, China). Venom components were eluted with a linear acetonitrile gradient (0–60% acetonitrile/0.1% TFA in 60 min) at a flow rate of 3.0 mL/min. The peak containing JZTx-27 was collected,

lyophilized, and purified to homogeneity by analytical RP-HPLC (C18 column, 5 μm, 4.6 × 250 mm; Welch Materials, Inc.).

Constructs and transfection

cDNA of sodium channels from *Paracoccus zeaxanthinifaciens* (Na_vPZ) and *Silicibacter pomeroyi* (Na_vSP), Ns_vBa and bacterial sodium channel from *Bacillus halodurans* (NaChBac) were cloned into a pTracer-CMV2 plasmid containing an enhanced green fluorescent protein that enables the confirmation of the transfected cells (12). Mutant and chimeric channels were generated with a QuickChange II XL Site-Directed Mutagenesis Kit (Agilent Technologies, Palo Alto, CA, USA) according to the manufacturer's instructions. Na_v1.5-Na_v1.8 chimeric channels were constructed by replacing human (h)Na_v1.5 domains with those of rat (r)Na_v1.8 by using a recombination strategy, as described in our previous study (23). Primers used for the linearization of hNa_v1.5 channel were as reported (23), whereas rNa_v1.8 transmembrane domains were amplified using the following primers. rNa_v1.8 domain I: forward primer 5'–AGAGCGGCTGTGAAGGTGTCGTCCATTCCTGGTCTCCAT–3', reverse primer 5'–GTTTGTCTCCATACCGCATGGTGACCACGGCCAAGATCAAAT–3'; rNa_v1.8 domain II: forward primer 5'–AAGCAGGGAGTGAAGGAGCTGGTACTGACCCCTTCGCAGA–3', reverse primer 5'–TGCACTGAAGGAGCTCAGCAGTAAAGCGATGAAAA-GGTTGA–3'; rNa_v1.8 DIII: forward primer 5'–AAGA-CCTGCTACCACATCGTGGAGCACAGCTGGTTTGAGAGT–3', reverse primer 5'–TTGGTTGAAGTTGTCGATTATGACCCCAACAAAGAGATTC–3'; and rNa_v1.8 domain IV: forward primer 5'–GCCTTCATATTCGACATCGTGA–3', reverse primer 5'–CACGCTGAAGTTCTCAGAATCACTGCGATGTACATGTTGACCAC–3'. The joint sequences are underlined. Primers were designed with Primer Premier 5.0 software and were synthesized in Genscript (Genscript Corp., Nanjing, China). All constructs were sequenced to confirm that the appropriate mutations/chimeras had been made. Transfections of wild-type (WT), mutant, or chimeric channels into CHO-K1, ND7/23, and HEK293T cells were performed by using Lipofectamine 2000 (Thermo Fisher Scientific, Waltham, MA, USA), according to the manufacturer's instruction. Six hours after transfection, the cells were seeded onto a glass coverslip (Thermo Fisher Scientific), and 24 h after seeding, they were ready for patch-clamp analysis.

Electrophysiological analysis

Cells transfected with WT/mutant/chimeric channels seeded in a glass coverslip were placed in a perfusion chamber, in most cases, rapid exchange of the bath solutions around the cells was performed (24). For determining the binding kinetic of toxin with channel, toxin was applied by a pipet located close to the recording cell to achieve fast solution exchange. For electrophysiological recording, the pipet solution contained 27 mM CsCl, 120 mM methane sulfonate, 8 mM NaCl, 10 mM EGTA, 2 mM Mg-ATP, and 20 mM HEPES (pH = 7.4). The bath solution contained 140 mM NaCl, 2 mM CaCl₂, 1 mM MgCl₂, 5 mM KCl, 20 mM HEPES (pH = 7.4), and 10 mM glucose. All experiments were conducted at room temperature (20–25°C). All chemicals were products of Sigma-Aldrich (St. Louis, MO, USA) and dissolved in sterile double-distilled H₂O. Data were collected by the PatchMaster software in an HEKA EPC-10 USB patch-clamp system (HEKA Elektronik, Ludwigshafen, Germany) and analyzed by Igo Pro-6.00, Prism (GraphPad Software, La Jolla, CA, USA), Sigmaplot 10.0 (Systat Software, Inc., San Jose, CA, USA), and OriginPro

8 (Northampton, MA, USA); voltage errors were minimized by using 80% series resistance compensation; and the capacitance artifact was canceled by using the computer-controlled circuitry of the patch-clamp amplifier. The dose-response curves of the toxin on WT, chimeric, and mutant channels were fitted to a Hill equation to estimate the potency of the toxin (IC_{50}). The $G-V$ and SSI curves were fitted by using a Boltzmann equation (Eq. 1):

$$y = y_{\text{steady}} + (y_{(0)} - y_{\text{steady}})/(1 + \exp[(V - V_{1/2})/K]) \quad (1)$$

where $V_{1/2}$, V , and K represents midpoint voltage of activation or inactivation, test potential, and slope factor, respectively. The current recovery of NS_VBa and $NaChBac$ upon washing off the toxin were fitted by Eq. 2:

$$y = y_{(0)} + a(1 - e^{-x/\tau}) \quad (2)$$

the decreases in NS_VBa and $NaChBac$ currents after toxin application were fitted by Eq. 3:

$$y = y_{\text{steady}} + ae^{-x/\tau} \quad (3)$$

where τ represents the time constant. Free energy of toxin-channel association was derived from Eq. 4:

$$\Delta G = -RT \ln(IC_{50}) \quad (4)$$

where IC_{50} , R , and T are half maximal inhibitory concentration, the universal gas constant and absolute temperature, respectively.

Statistics

Data are presented as means \pm SD; n = separate experimental cells. Statistical significance was assessed with GraphPad Prism using the paired Student's t test or 1-way ANOVA. Statistical significance was accepted at $P < 0.05$.

Structural modeling of NS_VBa -JZTx-27 complex

Homology modeling of NS_VBa voltage-sensing module (VSM) was performed with Rosetta cyclic coordinate descent (25) and kinematic (26) loop modeling applications with membrane-environment-specific energy function (27–29) and a bacterial Na_VAb channel structure (Protein Database ID: 3RVY) (7) as a template. The activated-state NS_VBa VSM model was generated by sequence alignment with the Na_VAb VSM. The resting-state models of NS_VBa were generated by shifting the NS_VBa S4 sequence down by 3 (resting state 2) or 6 (resting state 1) residue positions, with respect to the Na_VAb S4 sequence, to simulate a 1- or 2-helix-turn sliding transition of the S4 gating-charge-carrying arginines from the activated to the deactivated state (27, 30). The S1-2 and S3-4 loops were rebuilt *de novo*. For each VSM state, 20,000 models were generated, and the 1000 best scoring models were clustered to identify the most frequently sampled conformations. Models representing the top 20 clusters were visually evaluated based on experimental data to select the best models for toxin docking. Homology models of JZTx-27 were generated with the Rosetta Relax application (31), and the Huwentoxin-I NMR structure (ID: 1QK6) (32) served as a template. Docking of JZTx-27 models to the NS_VBa VSM models was performed with the Rosetta Dock application (33) with membrane-environment-specific energy function (27–29). For each toxin-channel pair, 10,000 other models were generated. The 1000 best scoring models were evaluated based on the difference in free energy between the unbound and bound states ($\Delta\Delta G$). The best 1,000 models by $\Delta\Delta G$ score were clustered, and the top 20 clusters were

evaluated based on agreement with experimental data to select the best models. Structural model of NS_VBa -JZTx-27 complex shown in Fig. 7 represents 1 of the top 20 clusters of NS_VBa in resting state 1. This model had the best agreement with the data, based on mapping of F98 and H102 at the channel-toxin interface.

RESULTS

Isolation and characterization of JZTx-27 as an antagonist of NS_VBa and $NaChBac$

To identify peptide modifiers of bacterial Na_Vs , we collected RP-HPLC fractions of venoms of several species of spider and tested their effect on Na^+ currents conducted by 4 bacterial Na_V channels: Na_VPZ , Na_VSP , NS_VBa , and $NaChBac$. We identified and purified a peptide (JZTx-27 or U24-theraphotoxin-Cg1a) from the venom of *Chilobrachys jingzhao* as an antagonist of NS_VBa and $NaChBac$ (Supplemental Fig. S1A, B). The molecular mass of JZTx-27 is 4086.81 Da ($M+H^+$), as determined by matrix-assisted laser desorption/ionization mass spectrometry (Supplemental Fig. S1D). The full amino acid sequence was determined by Edman degradation, which was also confirmed by its cDNA sequence (Supplemental Fig. S1C). The observed molecular mass of JZTx-27 (4085.81 Da) was 1 Da less than the theoretical one (4086.78 Da) based on the mature peptide sequence, indicating C-terminal amidation in the toxin to delete the C-terminal glycine residue in the propeptide (Supplemental Fig. S1C, D). This 34-residue peptide contains 6 cysteines whose localization was conserved among venom peptides containing an inhibitor cystine knot (ICK) motif (Fig. 1A). It was assumed that JZTx-27 would adopt the ICK scaffold and share the same disulfide linkage pattern (1–4, 2–5, and 3–6; the numbers indicate the relative positions of cysteines in the sequence). JZTx-27 inhibited Na^+ currents from the bacterial Na_Vs NS_VBa and $NaChBac$ (Fig. 1B, C), whereas little or no inhibition was observed for the Na_VPZ and Na_VSP channels (Fig. 1D, E). The inhibition of NS_VBa and $NaChBac$ currents by JZTx-27 was dose dependent. The IC_{50} was 112 nM for NS_VBa at the depolarizing voltage of 0 mV, and it was 30 nM for $NaChBac$ at the depolarizing voltage of -20 mV (Fig. 1F). These potencies translate to a very high energy of interaction between the sodium channels and the toxin ($\Delta G = -9.9$ kcal/mol and -10.7 kcal/mol for NS_VBa and $NaChBac$, respectively). The binding of JZTx-27 to the channel was very rapid ($\tau_{\text{on}} = 3.1 \pm 1.6$ s for NS_VBa and $\tau_{\text{on}} = 5.9 \pm 1.5$ s for $NaChBac$), whereas dissociation was relatively slow after toxin removal ($\tau_{\text{off}} = 41.8 \pm 5.4$ s for NS_VBa and $\tau_{\text{off}} = 105.8 \pm 2.4$ s for $NaChBac$; Fig. 1G).

Voltage-dependent inhibition of NS_VBa by JZTx-27

A common feature of Na_V gating modifier toxins is their ability to alter channel gating by trapping voltage sensors in a certain state, which affects voltage-dependent conformation transitions in response to membrane depolarizations. In contrast, pore blockers function by interacting with the outer or inner pore of Na_Vs . Although some pore

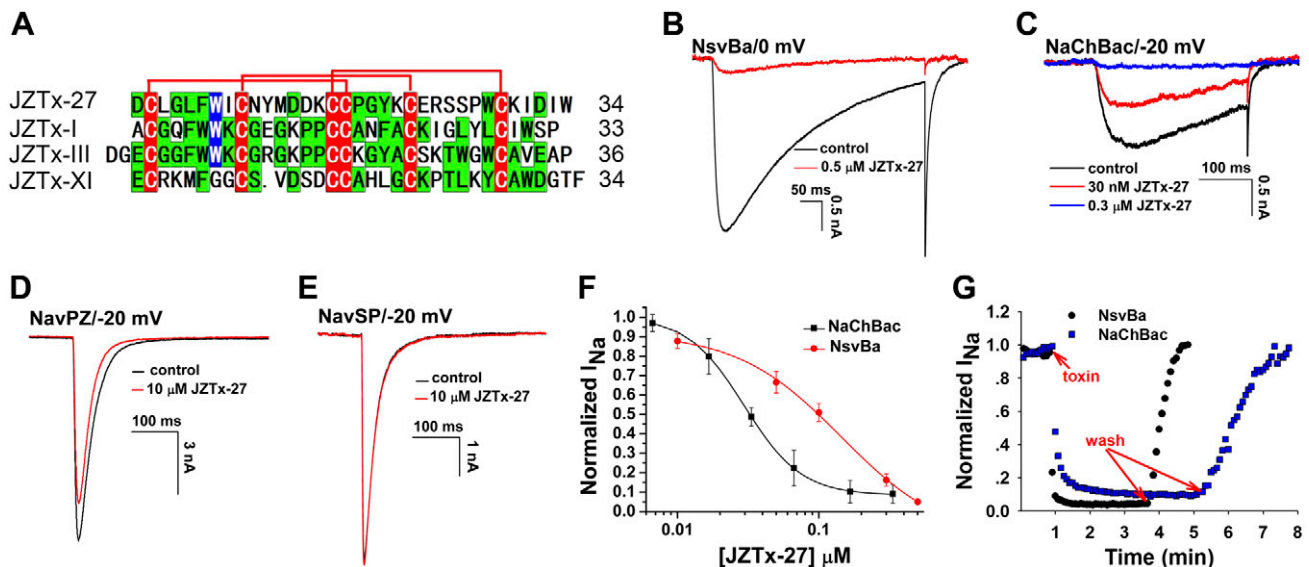


Figure 1. JZTx-27 antagonizes bacterial Nav_s. **A**) Sequence alignment of JZTx-27 with several ICK toxins; red lines show the disulfide linkage. **B, C**) JZTx-27 blocks the currents of NsvBa and NaChBac channels heterologously expressed in CHO-K1 cells ($n = 6-8$). **D, E**) NavPZ and NavSP channels were resistant to JZTx-27 ($n = 4$). **B-E**) currents were elicited by a 300 ms depolarization to 0 or -20 mV from a holding potential of -100 mV. **F**) Dose-dependent inhibition of NsvBa ($IC_{50} = 112$ nM) and NaChBac ($IC_{50} = 30$ nM) by JZTx-27 ($n = 6-8$). **G**) Time course for JZTx-27 blocking NsvBa ($0.5 \mu\text{M}$ toxin added) and NaChBac ($0.2 \mu\text{M}$ toxin added) and for recovery of their currents upon washing with bath solution ($\tau_{\text{on}} = 3.1 \pm 1.6$ s, $\tau_{\text{off}} = 41.8 \pm 5.4$ s for NsvBa; $\tau_{\text{on}} = 5.9 \pm 1.5$ s, $\tau_{\text{off}} = 105.8 \pm 2.4$ s for NaChBac; $n = 5$).

blockers were shown to affect the voltage-dependent activation or inactivation of Nav_s, the underlying mechanism may be an allosteric effect, not direct hindering or facilitating the voltage sensor movement (34). The Nav_s blocker lidocaine antagonizes NaChBac in a concentration range similar to resting blockage on eukaryotic Nav_s (35, 36). In the present study, the kinetics of NsvBa channel after treatment with lidocaine and JZTx-27 were analyzed and compared. We tested the activity of lidocaine on NsvBa and found that it dose dependently antagonized NsvBa with an affinity similar to NaChBac ($IC_{50} = 100 \mu\text{M}$; Supplemental Fig. S2A and Fig. 2E). As shown in Fig. 2A, B, 150 nM JZTx-27 and 100 μM lidocaine effectively inhibited NsvBa currents, whereas the current-voltage (I-V) relationship was the same as the control after lidocaine treatment, but it was positively shifted by JZTx-27 (Fig. 2A, B). In addition, the conductance-voltage (G-V) curves showed that the voltage-dependent activation of NsvBa was positively shifted by JZTx-27 but not by lidocaine (Fig. 2C and Supplemental Fig. S2B; $V_a = -20.6 \pm 9.8$ mV for control and $V_a = 8.4 \pm 7.0$ mV for 150 nM JZTx-27 treatment; $V_a = -20.6 \pm 8.3$ mV for control and $V_a = -20.5 \pm 9.2$ mV for 100 μM lidocaine treatment), which supports that JZTx-27 may act on NsvBa by modifying channel gating rather than physically blocking the pore.

The I-V curves in Fig. 2A clearly show that the JZTx-27 did not efficiently block NsvBa current at a depolarizing voltage of 40 mV, which suggests that the action of toxin on NsvBa channel is voltage dependent. At voltages evoking large inward NsvBa currents (from -20 to 30 mV), the inhibition of the NsvBa currents by 150 or 750 nM JZTx-27 was most pronounced at -20 mV, and the inhibition ratio decreased at more depolarized voltages (Fig. 2D). A higher dose of JZTx-27 (750 nM) resulted in much more inhibition

of NsvBa currents, but the slope of the curve was significantly smaller than that of 150 nM JZTx-27 ($K = 0.003 \pm 0.001$ and $K = 0.010 \pm 0.002$ for 750 nM and 150 nM JZTx-27, respectively; $P < 0.001$, 1-way ANOVA, $n = 5-9$; Fig. 2D), showing less dependence on voltage when saturating channels with toxins. The apparent affinity (IC_{50}) of JZTx-27 with NsvBa was 103 and 220 nM at 0 and 30 mV, respectively (Fig. 2E), whereas lidocaine exhibited nearly the same apparent affinity with NsvBa at 2 voltages ($IC_{50} \approx 100 \mu\text{M}$) (Fig. 2E). In addition, JZTx-27 did not change the steady-state inactivation of NsvBa markedly ($V_h = -52.7 \pm 5.9$ mV for control and $V_h = -52.1 \pm 5.7$ mV for 150 nM JZTx-27 treatment). These data suggested that the inhibition of NsvBa currents by JZTx-27 was voltage dependent, and the mechanism seemed to be the reopening of toxin-occupied channels, as judged from the distinct steady-state activation kinetics of NsvBa after JZTx-27 treatment.

JZTx-27 stabilizes NsvBa in the resting state

The interaction of peptide toxins with ion channels may be state dependent. To determine whether JZTx-27 prefers the NsvBa channel in one state in its gating pathway, the effects of JZTx-27 on the activation and deactivation of NsvBa channels were explored. The current of NsvBa was elicited by a 20 ms depolarization to 60 mV, followed by a -50 mV holding for 500 ms (tail voltage). This tail voltage was too weak to activate the closed NsvBa channels, and those already opened in the depolarization step were allowed to endure the deactivation process. Representative current traces in response to this voltage protocol are shown in Fig. 3A (inset). The activation phases of the outward currents before and after JZTx-27 or lidocaine

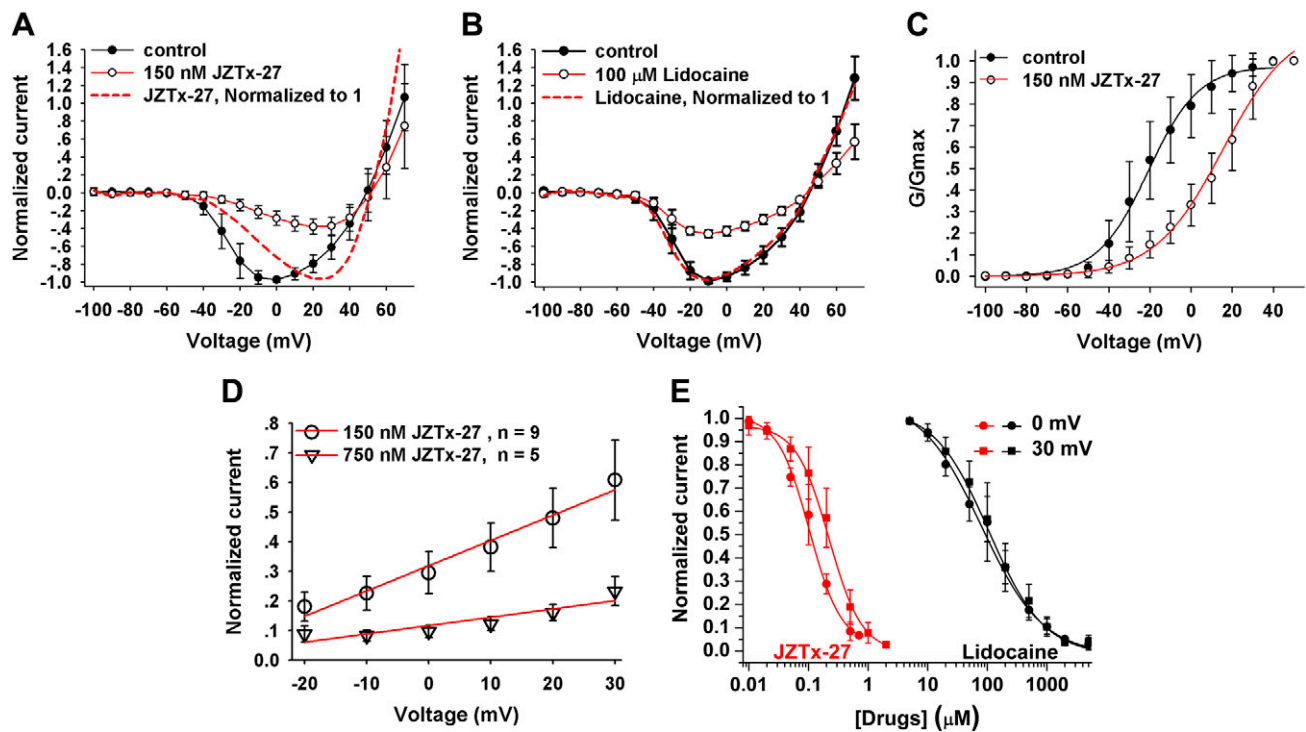


Figure 2. JZTx-27 antagonizes $N_{sv}Ba$ voltage dependently. *A, B*) I–V relationships of $N_{sv}Ba$ before and after treatment with JZTx-27 or lidocaine. Cells were held at -100 mV, and a cluster of depolarizing pulses (from -100 to 70 mV, in 10 mV increments) were applied. Currents evoked by different depolarizing voltages were normalized to the maximum peak current before drug treatment (solid lines). If currents from a drug-treated cell were normalized to its own maximum peak current (normalization to 1), the I–V curve is shown as the red dashed lines, which indicate the shape comparison of I–V curves from the control and the drug-treated channels ($n = 8-12$). *C*) The steady-state activation curve of $N_{sv}Ba$ was positively shifted by JZTx-27 ($V_a = -20.6 \pm 9.8$ mV for control and $V_a = 8.4 \pm 7.0$ mV for JZTx-27-treated $N_{sv}Ba$ channels; $n = 8-12$). *D*) In every depolarizing voltage (ranging from -20 to 30 mV), the $N_{sv}Ba$ current after 150 or 750 nM JZTx-27 treatment was normalized to that before drug application and plotted, showing voltage-dependent inhibition of $N_{sv}Ba$ by JZTx-27 ($n = 5-9$). *E*) Dose–response curves for JZTx-27 or lidocaine blocking $N_{sv}Ba$ currents, IC_{50} were determined as 103 nM and 220 nM for JZTx-27 and ≈ 100 μM for lidocaine, at 0 and 30 mV, respectively ($n = 7-9$).

treatment were fitted as shown in Fig. 3A, B, and the activation time constant ($\tau_{activation}$) was calculated. The $\tau_{activation}$ of $N_{sv}Ba$ channel before and after 150 nM JZTx-27 treatment was determined to be 2.9 ± 0.7 and 5.5 ± 1.6 ms, respectively, showing a significant slowing of channel activation by toxin (representative traces in Fig. 3A and statistics in Fig. 3C). We also tested a higher dose of toxin, 750 nM JZTx-27, which increased the $\tau_{activation}$ significantly as well (Fig. 3C, $\tau_{activation} = 3.4 \pm 0.5$ ms for control and $\tau_{activation} = 6.2 \pm 1.7$ ms for toxin treatment). In contrast, as shown in Fig. 3B, traces before and after the 50 - μM lidocaine treatment were superimposed, suggesting no alteration of the $N_{sv}Ba$ activation by lidocaine. Data in Fig. 3C also show that the $\tau_{activation}$ of $N_{sv}Ba$ channels after varied doses of lidocaine treatment (20 μM , 50 μM , and 1 mM) were not greatly changed when compared with that of the control. This evidence, as well as the unaltered I–V relationship of $N_{sv}Ba$ by lidocaine treatment, strongly suggests that the residual currents after lidocaine treatment are contributed by the population of lidocaine-free channels. Another characteristic of $N_{sv}Ba$ after JZTx-27 treatment is that channels deactivated much faster than that of the control, as shown by normalizing the tail current magnitudes in Fig. 3D. Fitting the falling phase of the tail currents showed the $\tau_{deactivation}$ to be 57.3 ± 14.8 ms for

control and 30.2 ± 15.2 ms for 150 nM toxin-treated channels (Fig. 3D). 750 nM JZTx-27 also reduced the deactivation time constant from 57.7 ± 15.2 to 15.2 ± 5.0 ms (Fig. 3D). These data suggest that toxin remains bound to $N_{sv}Ba$ channel during the activation and the deactivation process, altering the kinetics of channel state transition.

We further compared the effects of JZTx-27 and lidocaine on $N_{sv}Ba$ channel activation at much stronger depolarizations. Cells were held at -100 mV and $N_{sv}Ba$ channels were activated by applying a series of 20 ms depolarizations ranging from 60 to 100 mV (10 mV/step), followed by a -50 mV holding of tail voltage for 500 ms. The change of the tail current amplitudes in response to the depolarizations (60 – 100 mV) reflects the change of the number of activated channels. As shown in Fig. 3E, at the voltages tested, the activation of $N_{sv}Ba$ was significantly slowed by 750 nM JZTx-27: $\tau_{activation} = 2.6 \pm 0.3$ ms for control and 5.6 ± 1.8 ms for toxin treatment at 70 mV; 2.1 ± 0.3 ms for control and 4.9 ± 1.7 ms for toxin treatment at 80 mV; 1.7 ± 0.4 ms for control and 4.4 ± 1.7 ms for toxin treatment at 90 mV; and 1.4 ± 0.3 ms for control and 3.9 ± 1.7 ms for toxin treatment at 100 mV. However, 1 mM lidocaine did not markedly alter the activation of $N_{sv}Ba$ at every depolarizing voltage (Fig. 3F). The traces in Fig. 3G showed the tail currents from 2 representative cells in

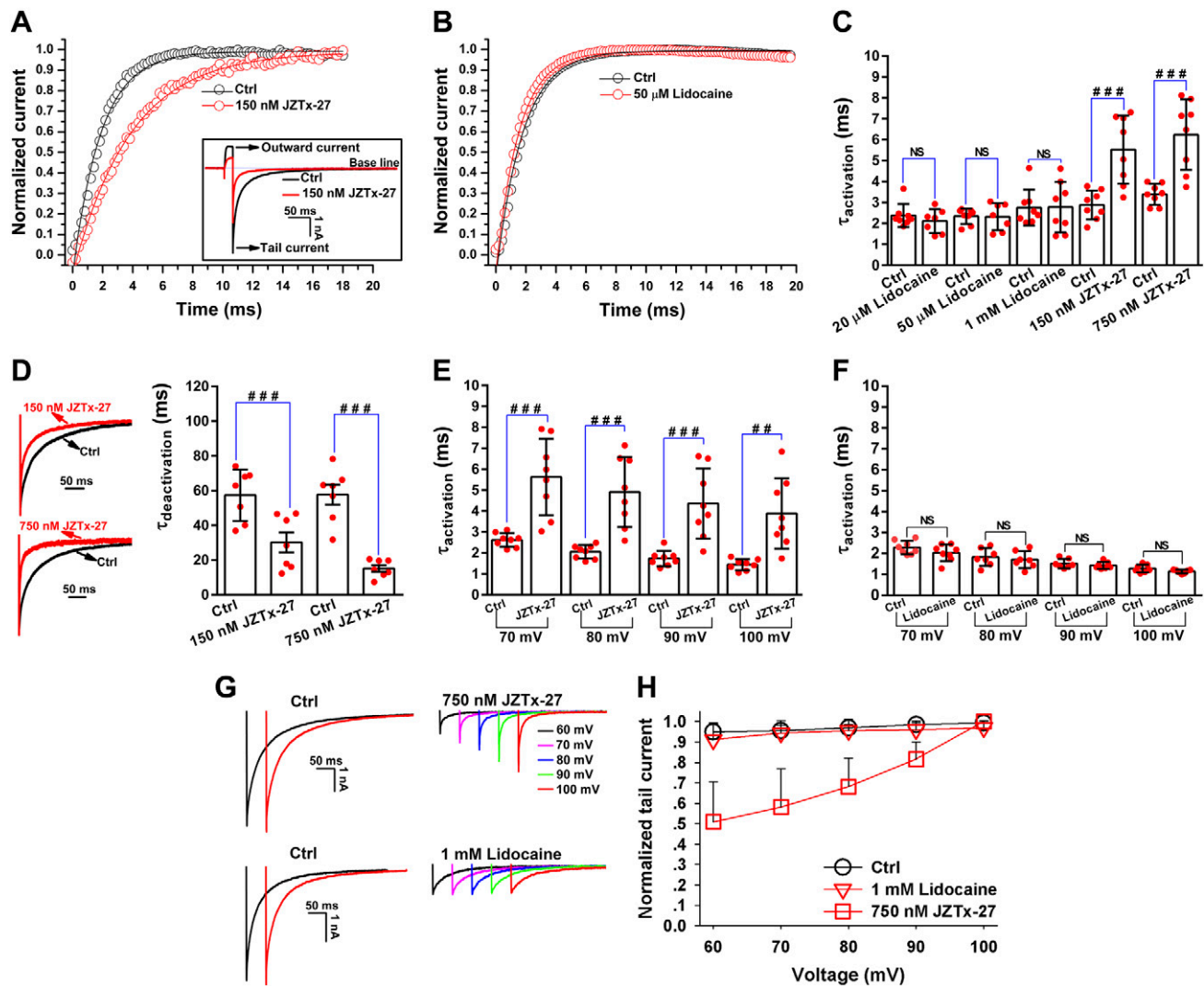


Figure 3. JZTx-27 stabilizes NsvBa in the resting state. *A, B*), Currents (*A*, inset) were elicited by a 20 ms depolarization to 60 mV, followed by a 500 ms tail-voltage holding at -50 mV. The $\tau_{\text{activation}}$ were determined by fitting the activation phases of the outward currents with an exponential rising equation. *C*) The bar diagram shows the comparison of $\tau_{\text{activation}}$ values for control and channels treated with varied doses of lidocaine or JZTx-27 ($n = 8$). $###P < 0.001$ (paired Student's *t* test). NS, not significant. *D*) Left: representative normalized NsvBa tail currents show that JZTx-27 accelerated channel deactivation. Tail currents were elicited as described in (*A*). The $\tau_{\text{deactivation}}$ was determined by fitting the decay phase of the tail current with a single exponential equation, and results are compared in the right panel ($n = 7$ for each group). $###P < 0.001$ (paired Student's *t* test). *E, F*) The comparison of $\tau_{\text{activation}}$ values for control and drug-treated channels at depolarizing voltages ranging from 70 to 100 mV ($n = 7-8$). $##P < 0.01$, $###P < 0.001$ (paired Student's *t* test). *G*) NsvBa tail currents were elicited by depolarizations from 60 to 100 mV, followed by a 500 ms tail-voltage holding at -50 mV. Enhancing depolarizations increased tail current amplitude in the JZTx-27 group but not in the control or lidocaine group. *H*) For every tested cell in *G*, the tail currents evoked by different depolarizations were normalized to that by 100 mV and plotted. Data are means \pm SD ($n = 7-10$). *C-F*) The individual red dot above each column represents the $\tau_{\text{activation}}$ or $\tau_{\text{deactivation}}$ value from a single experimental cell.

response to voltage protocol described. In the control and the lidocaine groups (Fig. 3*G*), the tail current amplitudes of NsvBa at 60 and 100 mV depolarizations were almost the same, indicating that all channels available in the membrane were activated at 60 mV. However, the amplitudes of tail currents increased with the increment of depolarizing voltages in cells treated with JZTx-27 (Fig. 3*G*), indicating more toxin-occupied channels were activated by strengthening depolarization (see also statistics in Fig. 3*H*).

These data show that the activation of NsvBa was significantly slowed by JZTx-27 and that the toxin-occupied channels required much stronger depolarization to be

activated and display accelerated deactivation, which suggests that JZTx-27 traps NsvBa in the resting state. We proposed that the toxin delays the closed-to-open state transition, possibly by trapping the deactivated state of the voltage sensor.

JZTx-27 interacts with the S3-4 extracellular loop of NsvBa channel

Our data suggest that JZTx-27 acts as a gating modifier, sharing a similar manner of action with some mammalian

Nav_s site 4 toxins which cause a positive shift of the steady-state activation. These toxins are proposed to bind to the voltage sensor of Nav_s by interacting with the S1-2 and S3-4 extracellular loops, where voltage-dependent movement of the S4 voltage sensor is impaired. To test this hypothesis, we constructed NsvBa chimeric channels by replacing its S1-2 (chimera 1) and S3-4 (chimera 2) extracellular loops with those of Nav_vPZ (Figs. 4A and 5A). chimera 2 but not chimera 1 was functionally expressed in CHO-K1 cells (Fig. 4B). The affinity of JZTx-27 with chimera 2 was dramatically reduced when compared to WT channel as 3 μM toxin only inhibited its peak current by 19.4 ± 3.6% (Fig. 4B, C). The apparent IC₅₀ of JZTx-27 on chimera 2 was assessed at the voltage evoking its maximum peak current (Fig. 4C). These data highlight the crucial role of S3-4 loop of NsvBa in determining the JZTx-27-NsvBa interaction.

F98 in NsvBa is critical for JZTx-27-channel interaction

To determine the key amino acids responsible for JZTx-27-NsvBa interaction, we used scanning mutagenesis of the S1-2 and S3-4 loops. Because some mutations altered channel activation kinetics, the apparent IC₅₀ of JZTx-27 against each mutant was measured at the voltage for their maximum peak current (Supplemental Table S1). Each amino acid positioned in the S3-4 loop of NsvBa was substituted with the corresponding residue found in Nav_vPZ (see sequence alignment shown in Fig. 5A). The IC₅₀ of JZTx-27 on the F98P mutant could not be determined, as high-dose toxin (3 μM) inhibited the sodium current by less than 20% (Fig. 5B, C). Mutations F98A and H102Q reduced JZTx-27 potency ~3–6-fold, whereas F98L mutation did not significantly change the sensitivity of NsvBa to JZTx-27 (Fig. 5D). Because the NsvBa/Nav_vPZ S1-2 loop chimera (chimera 1) did not functionally express, we alanine scanned residues within the S1-2 loop, as well as the S3b paddle motif. All of these mutations reduced the affinity of JZTx-27 with NsvBa by less than 3-fold when

compared to WT channel. These data suggest that the S3-4 loop of NsvBa forms a key receptor site for JZTx-27. Taking into account the disruptive effect of F98P mutation on the spatial organization of the S3-4 loop, we further tested the effect of mutating a conserved F103 (analogous to F98 in NsvBa) in NaChBac on the affinity of toxin with channel. Consistent with the NsvBa F98P mutant, the NaChBac F103P mutant was resistant to JZTx-27 treatment with 1.5 μM toxin inhibiting little of its peak current (Fig. 5E). However, in contrast to NsvBa F98A and NsvBa F98L mutants, the affinity of JZTx-27 to NaChBac F103A mutant was reduced by ~10-fold when compared with that of the WT channel (Fig. 5E, F; IC₅₀ = 30 nM and 308 nM for WTNaChBac and NaChBac F103A mutant, respectively). These data validate the critical role of F98 in NsvBa in the interaction of toxin with channel. The observation that mutating F98 to alanine (F98A) or leucine (F98L) in NsvBa barely affected the affinity of toxin with channels may be explained by a compensatory binding site for JZTx-27 in the channel sequence.

The effect of JZTx-27 on mammalian Nav_s

The activity of JZTx-27 on endogenous sodium currents from rat dorsal root ganglion (DRG TTX-R I_{Na}) and on 6 heterologously expressed mammalian Nav_v subtypes (hNav_v1.1, hNav_v1.3, rNav_v1.4, hNav_v1.5, hNav_v1.7, and rNav_v1.8) were assessed. The endogenous DRG TTX-R Na⁺ channels, hNav_v1.1 and rNav_v1.8, were resistant to JZTx-27 (Fig. 6A, C). However, JZTx-27 antagonized the peak currents as well as the inactivation of hNav_v1.3, rNav_v1.4, hNav_v1.5, and hNav_v1.7 (Fig. 6A). Of the Nav_v subtypes tested, hNav_v1.5 exhibited the greatest sensitivity to JZTx-27, with an EC₅₀ of 700 nM (measured by the I_{5ms}:I_{peak} ratio; Fig. 6B). Nav_v chimeras were constructed to explore the primary receptor site in hNav_v1.5 for JZTx-27. Functional channels were constructed by replacing DII, DIII, and DIV, but not DI, of hNav_v1.5 with those of rNav_v1.8 [Fig. 6D–F, referred to as DII (Nav_v1.8), DIII (Nav_v1.8), and DIV

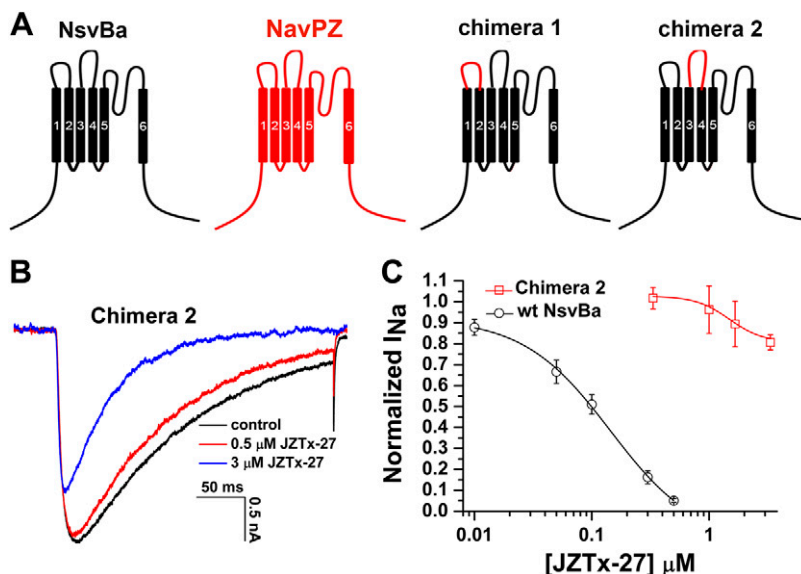


Figure 4. Determination of the key region in NsvBa for binding JZTx-27. A) The strategy for NsvBa/Nav_vPZ chimera construction. B) Representative traces showed that chimera 2 was resistant to JZTx-27 compared with the WT NsvBa channel ($n = 4-6$). C) Dose-response curves show that replacing NsvBa S3-4 extracellular loop with that of Nav_vPZ (chimera 2) attenuated toxin affinity, with 3 μM JZTx-27 inhibiting its peak current by only 19.4 ± 3.6% ($n = 5-8$).

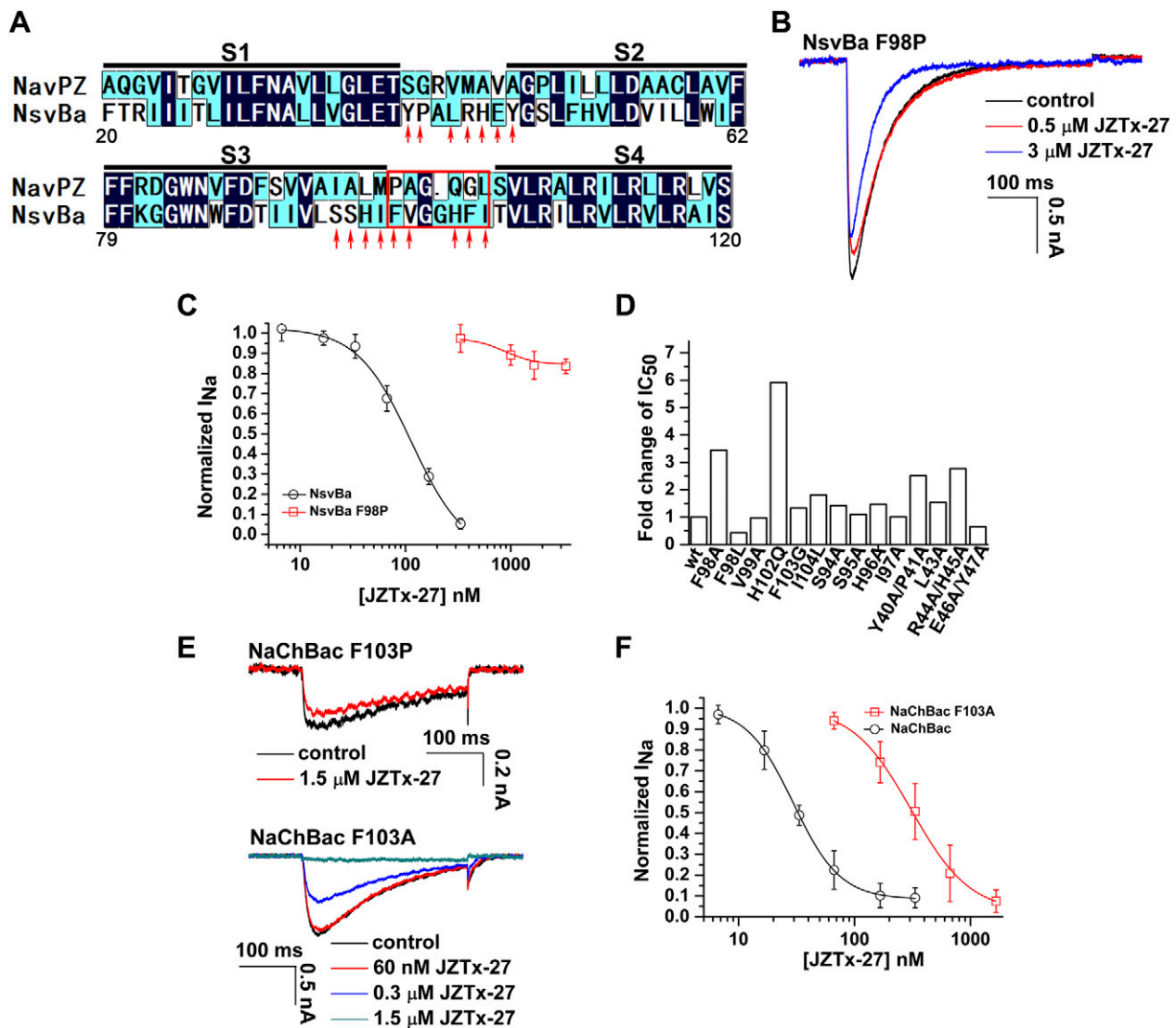


Figure 5. Effect of JZTx-27 on NsvBa and NaChBac mutants. *A*) Sequence alignment of multiple bacterial Navs (NavRh, NavPZ, NaChBac, NavAb, and NsvBa) determined the S1-2 and S3-4 extracellular loops (cluster Omega). For clarity, only NavPZ and NsvBa are shown. Red arrows: the mutated residues in NsvBa. *B*) Representative traces show that the NsvBa F98P mutant was resistant to JZTx-27. *C*) Dose–response curves for JZTx-27 blocking WT-NsvBa and NsvBa F98P mutant; 3 μM toxin inhibited F98P mutant peak current by $16.4 \pm 3.6\%$ ($n = 5-7$). *D*) Fold changes in apparent toxin affinity ($\text{IC}_{50}^{\text{mutt}}/\text{IC}_{50}^{\text{wt}}$) were plotted for individual mutants. Note all IC_{50} values were determined at the depolarizing voltage evoking the maximum peak current of each mutant. For residues in the S1-2 loop (Y40, P41, L43, R44, H45, E46, and Y47) and S3b paddle motif (S94, S95, H96, and I97), an alanine scan strategy was used. Residues in the S3–4 loop were mutated to the corresponding ones in NavPZ ($n = 5-8$). *E*) NaChBac F103P and F103A mutants were differently resistant to JZTx-27 when compared with WT channel. *F*) Dose–response curves for JZTx-27 blocking NaChBac and NaChBac F103A mutant ($\text{IC}_{50} = 30$ nM for WTNaChBac and $\text{IC}_{50} = 308$ nM for NaChBac F103A mutant, respectively).

(Nav1.8), respectively]. Currents of each chimera were elicited by depolarization to 10 mV from a holding potential of -80 mV. DII (Nav1.8) chimera responded robustly to JZTx-27, with 1 μM toxin inhibiting its inactivation and activating its peak current (Fig. 6D); DIII (Nav1.8) chimera was sensitive; but DIV (Nav1.8) chimera was resistant to JZTx-27 (Fig. 6E, F), which suggests that the primary toxin binding site for JZTx-27 is located in DIV of Nav1.5. In contrast to Nav1.5, JZTx-27 activated the peak current of DII (Nav1.8) and did not affect that of DIII (Nav1.8), suggesting multiple binding sites in hNav1.5 for JZTx-27. In addition, the activation of the peak current of DII (Nav1.8) by JZTx-27 may be partially contributed by toxin rendering DII (Nav1.8)

refractive to inactivation by positively shifting its steady-state inactivation (Supplemental Fig. S3). JZTx-27 could partially resemble α -scorpion toxins in acting on mammalian Navs, in stabilizing the deactivated voltage sensor of DIV to reduce the rate of channels' inactivation.

Structural model of JZTx-27 interaction with NsvBa voltage sensor

We used Rosetta structural modeling software to dock JZTx-27 to multiple states of the NsvBa VSM. Based on experimental data presented in this study (Fig. 5D),

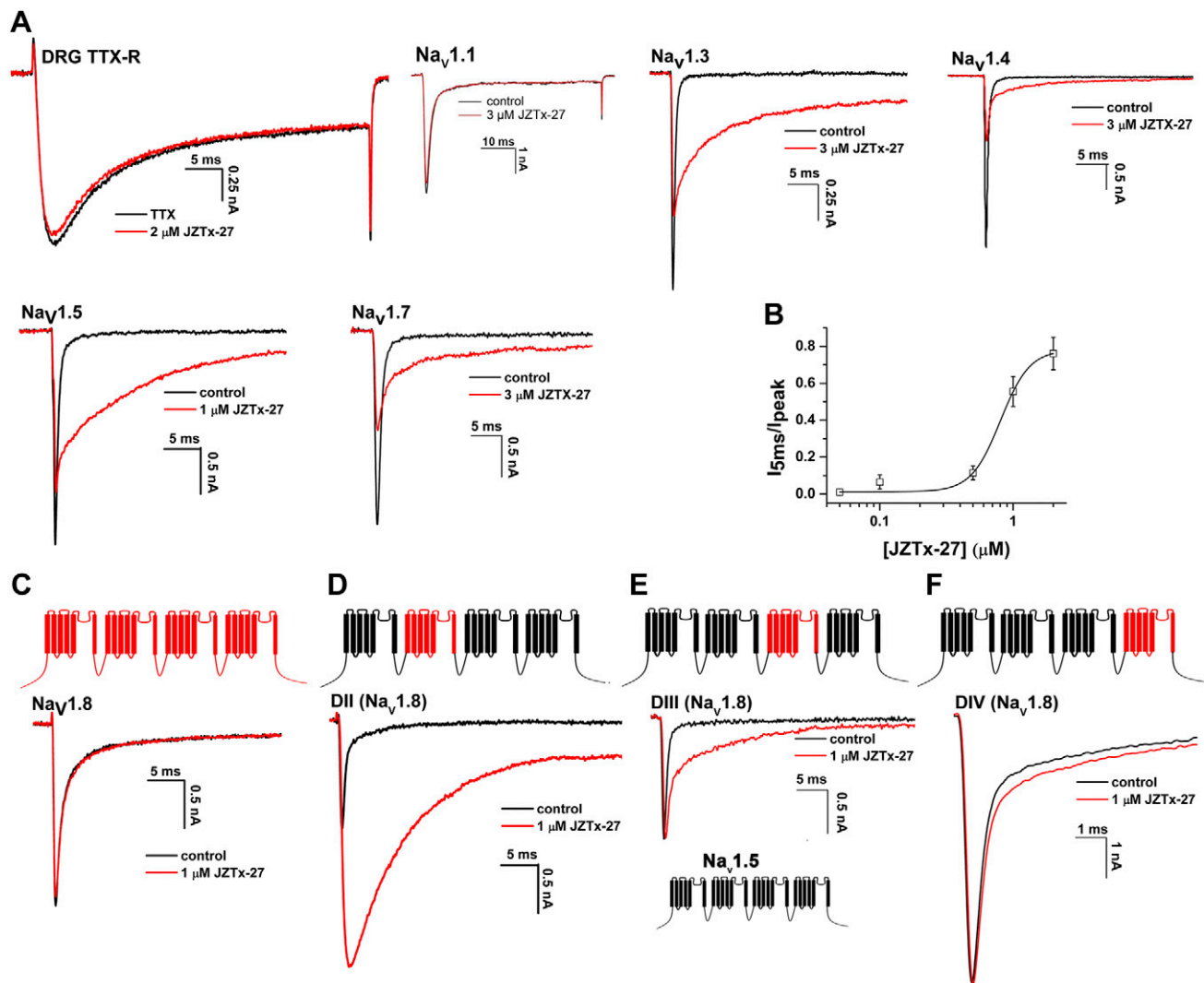


Figure 6. JZTx-27 targets domain IV of mammalian Navs. *A*) JZTx-27 inhibited the peak currents of Nav1.3-1.5 and Nav1.7 and slowed their fast inactivation. DRG TTX-R Navs and Nav1.1 were resistant to toxin ($n = 4-6$). *B*) The EC_{50} of JZTx-27 on Nav1.5 measured by the $I_{5ms}:I_{peak}$ ratio was determined as 700 nM ($n = 5$). *C*) Representative current traces show that Nav1.8 was resistant to JZTx-27 ($n = 5$). Nav1.8 (*C*) and Nav1.5 (*E*) are shown in red and black tracings, respectively. *D-F*) Chimeric channels were constructed by replacing DII [DII (Nav1.8)], DIII [DIII (Nav1.8)] and DIV [DIV (Nav1.8)] of Nav1.5 with those of Nav1.8. JZTx-27 inhibited the fast inactivation of DII (Nav1.8) and DIII (Nav1.8), but not of DIV (Nav1.8).

mutations of the S3-4 loop residues F98 and H102 had the biggest effect on JZTx-27 binding. **Figure 7** shows one of the most energetically favorable models of JZTx-27 in complex with Ns_VBa VSM in deactivated state 1, which has F98 and H102 at the toxin-channel interface. F98 on the channel is in proximity to F6 and W28 on the toxin, and H102 on the channel is in proximity to K30, D32, and I33 on the toxin. Experimental data also show a 2-3-fold change in IC_{50} for Y40A/P41A and R44A/H45A Ns_VBa double-site mutants (Fig. 5D). Y40 and H45 sidechains are pointing away from the toxin in our model (not shown). P41 is in proximity to W34 on the toxin in our model (Fig. 7), but the P41A mutant may also affect the secondary structure of the S1-2 loop and therefore reduce toxin binding. R44 is in proximity to D32 on the toxin in our model. Our model also suggests that G100 and G101 within the S3-4 loop of Ns_VBa allows for shape complementarity of C-terminal region

of the toxin. None of the top 20 clusters of the Ns_VBa-JZTx-27 complex in activated or deactivated state 2 (Supplemental Fig. S4) captured F98 and H102 at the channel-toxin interface.

DISCUSSION

JZTx-27 stabilizes the resting conformation of Ns_VBa

The voltage sensor-trapping model is a common mechanism underlying gating-modifier peptide toxins acting on voltage-gated ion channels (16). These toxins bind to the extracellular loops and trap the voltage sensors in a certain conformation, affecting the channels' gating kinetics. In the present study, JZTx-27 trapped Ns_VBa VSM in the deactivated state and consequently rendered the channel

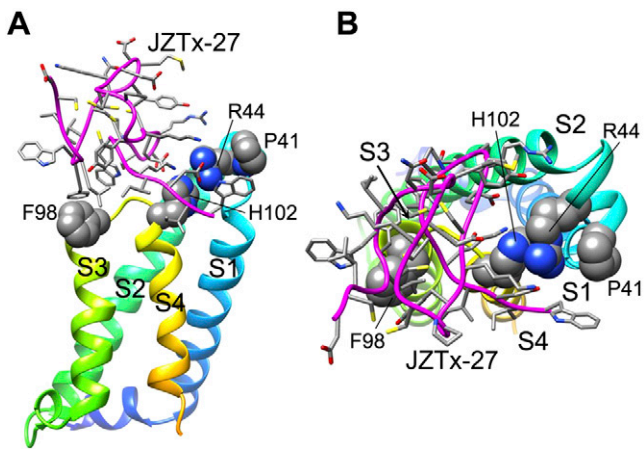


Figure 7. Structural model of the NsV Ba–JZTx-27 complex. *A*) Transmembrane view of the Rosetta model of resting-state NsV Ba in complex with JZTx-27. NsV Ba transmembrane segments S1–4 are colored with a rainbow scheme from blue to red and labeled accordingly. The carbon-chain of JZTx-27 is magenta. Side chains of key NsV Ba residues are shown in space-filling representations. Side chains of all residues on JZTx-27 are shown in stick representations. *B*) View of the model shown in *A* from the extracellular side of the membrane.

refractory to be activated by depolarization. Our conclusion is based on the following observations: 1) JZTx-27 blocks NsV Ba voltage dependently, with less inhibition at more depolarized voltages, and positively shifts the steady-state activation (Fig. 2); 2) the toxin-occupied channels can be reopened with decelerated activation but accelerates deactivation kinetics when compared with toxin-unoccupied channels (Fig. 3); and 3) the activation of toxin-occupied channels requires much stronger depolarization (Fig. 3). In contrast, lidocaine-treated NsV Ba channels did not have these gating properties. This difference may originate from the different molecular mechanisms by which they block NsV Ba. JZTx-27 directly interacted with the S3-4 extracellular loop of NsV Ba to impede VSM activation, and enhanced depolarization could have triggered the outward movement of the toxin-VSM complex to reopen the channel, whereas lidocaine antagonized NaChBac by stabilizing channels in the inactivated state (35). Furthermore, the binding site of lidocaine in bacterial Na_vs may partly overlap with P11, whose binding area in Na_vMs was determined to be the pore cavity region (37). One possibility is that lidocaine interacts with the pore of NsV Ba to stabilize the inactivated state, hence the lidocaine-bound NsV Ba channels could not be activated by simply driving outward movement of the voltage sensors by strengthening depolarizations. The observation that JZTx-27 significantly accelerates the deactivation of NsV Ba suggests that toxin-occupied channels also contribute to the tail current elicited by tail-voltage holding after strong depolarization (Fig. 3D), which indicates that the toxin forms a stable complex with the deactivated NsV Ba voltage sensor. In other words, NsV Ba voltage sensor activation is impeded, but its deactivation is facilitated by the cargo toxin, which is reminiscent of hanatoxin's effect on the Kv2.1 channel (38–40).

Our structural model of JZTx-27–NsV Ba voltage sensor interaction suggests that the hydrophobic surface of the toxin interacts with the membrane and S3-4 loop of the channel. The Rosetta model predicts that NsV Ba residues F98 and H102 interact with several residues on the toxin and that the S3-4 loop has significant shape complementarity with the C-terminal region of the toxin. The activated and deactivated state 2 of the NsV Ba VSM showed significantly different conformation of the S3-4 loop region (Supplemental Fig. S4). We suggest that in addition to interactions between JZTx-27 and F98 and H102 on the NsV Ba VSM, shape complementarity between the JZTx-27 and NsV Ba VSM S3-4 loop region plays an important role in stabilization of the specific NsV Ba VSM deactivated state upon JZTx-27 binding.

A homologous neurotoxin binding site in mammalian and bacterial Na_vs

Eight neurotoxin binding sites have been characterized in mammalian Na_vs (41). However, little is known about whether peptide toxin binding sites are conserved in prokaryotic Na_vs. Previous studies showed that local anesthetics inhibit bacterial Na_vs as well as their mammalian counterparts (35); fenestration between adjacent subunits of bacterial Na_vs provides an entry route for small neutral or hydrophobic drugs (22, 42, 43). The present study proved that the S3-4 extracellular loop of NsV Ba channel is the primary receptor site for JZTx-27, which is the first report that there is a mammalian Na_vs homologous peptide toxin binding site in bacterial Na_vs. Of the 8 neurotoxin-binding sites in mammalian Na_vs, site 3 and 4 are composed of extracellular loops of domains IV and II, respectively. Peptide toxins targeting sites 3 and 4 affect channel activation and inactivation, respectively (41). The effect of JZTx-27 on mammalian Na_vs was similar to α -scorpion toxins. Using Na_v chimeras, we have clearly demonstrated that JZTx-27 targets DIV of Na_v1.5 (Fig. 6D–F). The different responses of mammalian Na_vs and bacterial Na_vs to JZTx-27 resemble that of Na_v1.5 and Kv2.1 to JZTx-I (44, 45) and can be interpreted as follows: JZTx-27 targets the DIV VSM of mammalian Na_vs that is responsible for inactivation (46–49). However, bacterial Na_vs are homotetramers that lack a fast inactivation gate structure and a fast inactivation process. JZTx-27 traps the bacterial NsV Ba VSM in the deactivated state leading to inhibition of peak current.

JZTx-27 as a probe for the determination of NsV Ba structure in the resting state

Many neurotoxins bind to ion channels and trap them in specific states. This feature is useful for ion channel structure determination, as channel-toxin complexes often immobilize/stabilize labile channel motifs that enhances their structural refinement. In some cases, channel-toxin complex structure determination can reveal the channel structure in states that could not be captured from unbound channels, such as those channel states found in the cocrystal structure of acid-sensing ion channel

(ASIC)-1a-psalmotoxin (50), ASIC1a-MitTx (51), or TRPV1-DkTx (52). The simpler bacterial Na_vs are used by biologists to understand the biophysical determinant of mammalian Na_v conformational changes and function (53). Comparing the Na_vMs open pore with that of Na_vAb closed-pore structures has defined the mechanism of pore–module opening and closing (8). Most recently, 4 Na⁺ occupancy sites (S₀–S₃) within the selectivity filter of Na_vMs has been resolved in a crystal structure (54), challenging the 3-site model (site_{OUT}, site_{CEN}, and site_{IN}) proposed from the unoccupied filter of the Na_vAb structure (7). Thus, it would be interesting to see whether or not toxin binding to the voltage sensor domain could alter Na⁺ occupancy within the selectivity filter. Such observations would undoubtedly enhance our understanding of mechanical communication between the voltage sensor and the ion conducting site found in the pore modules. Compared with potassium selectivity in K⁺-channels (55, 56), the mechanism of Na⁺-selectivity in Na⁺-channels remains poorly understood. Na_v-toxin complexes may provide a unique tool to determine which Na⁺ selectivity filter site are most effected by toxin binding and thus which sites are essential to sodium conductance. The X-ray crystal structures of the Na_vAb and Na_vRh channels have captured the VSM in 2 different activated states (7, 9). However, no structure with the voltage sensor in the deactivated state has been reported so far. Although interactions which stabilize the fourth transmembrane segment (S4) in the deactivated and activated states have been described by modeling and functional analysis (27, 57–59), the structure of a sodium channel with a deactivated voltage sensor would certainly provide additional insight. For example, a deactivated voltage sensor structure would set the lower limit of S4 movement during the activation process and define the level of hydration within the gating pore. Because the resting membrane potential is absent in crystallographic conditions (60), the resting state (which requires –100 mV of membrane potential) will continue to elude structural biologists unless an agent (such as a toxin or channel modifier) can be used to provide molecular constraints to capture this conformation. The tarantula toxin JZTx-27 is able to stabilize Ns_vBa channel in the resting state. Therefore, it can be used as a probe to determine the resting conformation of this channel in functional and structural assays. FJ

ACKNOWLEDGMENTS

This work was supported by the National Basic Research Program of China (973 Program; Grant 2010CB529801); the National Science Foundation Project (Grants 31370783 and 31370817 to Z.L.); and the Cooperative Innovation Center of Engineering and New Products for Developmental Biology of Hunan Province (Grant 20134486). The authors declare no conflicts of interest.

AUTHOR CONTRIBUTIONS

C. Tang and Z. Liu developed the concept and designed the study; C. Tang, X. Zhou, Y. Zhang, Z. Hu and C. Zhang performed the experimental studies and data acquisition;

P. T. Nguyen and V. Yarov-Yarovoy were responsible for the structure modeling; and C. Tang, Z. Liu, P. G. DeCaen, V. Yarov-Yarovoy, and S. Liang prepared the manuscript.

REFERENCES

- Meisler, M. H., and Kearney, J. A. (2005) Sodium channel mutations in epilepsy and other neurological disorders. *J. Clin. Invest.* **115**, 2010–2017
- George, A. L., Jr. (2005) Inherited disorders of voltage-gated sodium channels. *J. Clin. Invest.* **115**, 1990–1999
- Struyk, A. F., Scoggan, K. A., Bulman, D. E., and Cannon, S. C. (2000) The human skeletal muscle Na channel mutation R669H associated with hypokalemic periodic paralysis enhances slow inactivation. *J. Neurosci.* **20**, 8610–8617
- Spampanato, J., Escayg, A., Meisler, M. H., and Goldin, A. L. (2001) Functional effects of two voltage-gated sodium channel mutations that cause generalized epilepsy with febrile seizures plus type 2. *J. Neurosci.* **21**, 7481–7490
- Jurkat-Rott, K., Mitrovic, N., Hang, C., Kouzmekine, A., Iaizzo, P., Herzog, J., Lerche, H., Nicole, S., Vale-Santos, J., Chauveau, D., Fontaine, B., and Lehmann-Horn, F. (2000) Voltage-sensor sodium channel mutations cause hypokalemic periodic paralysis type 2 by enhanced inactivation and reduced current. *Proc. Natl. Acad. Sci. USA* **97**, 9549–9554
- Catterall, W. A. (2000) From ionic currents to molecular mechanisms: the structure and function of voltage-gated sodium channels. *Neuron* **26**, 13–25
- Payandeh, J., Scheuer, T., Zheng, N., and Catterall, W. A. (2011) The crystal structure of a voltage-gated sodium channel. *Nature* **475**, 353–358
- McCusker, E. C., Bagn eris, C., Naylor, C. E., Cole, A. R., D’Avanzo, N., Nichols, C. G., and Wallace, B. A. (2012) Structure of a bacterial voltage-gated sodium channel pore reveals mechanisms of opening and closing. *Nat. Commun.* **3**, 1102
- Zhang, X., Ren, W., DeCaen, P., Yan, C., Tao, X., Tang, L., Wang, J., Hasegawa, K., Kumasaka, T., He, J., Wang, J., Clapham, D. E., and Yan, N. (2012) Crystal structure of an orthologue of the NaChBac voltage-gated sodium channel. *Nature* **486**, 130–134
- Payandeh, J., Gamal El-Din, T. M., Scheuer, T., Zheng, N., and Catterall, W. A. (2012) Crystal structure of a voltage-gated sodium channel in two potentially inactivated states. *Nature* **486**, 135–139
- Corry, B., Lee, S., and Ahern, C. A. (2014) Pharmacological insights and quirks of bacterial sodium channels. *Handb. Exp. Pharmacol.* **221**, 251–267
- Koishi, R., Xu, H., Ren, D., Navarro, B., Spiller, B. W., Shi, Q., and Clapham, D. E. (2004) A superfamily of voltage-gated sodium channels in bacteria. *J. Biol. Chem.* **279**, 9532–9538
- Ren, D., Navarro, B., Xu, H., Yue, L., Shi, Q., and Clapham, D. E. (2001) A prokaryotic voltage-gated sodium channel. *Science* **294**, 2372–2375
- DeCaen, P. G., Takahashi, Y., Krulwich, T. A., Ito, M., and Clapham, D. E. (2014) Ionic selectivity and thermal adaptations within the voltage-gated sodium channel family of alkaliphilic *Bacillus*. *eLife* **3**, 3
- Terahara, N., Sano, M., and Ito, M. (2012) A *Bacillus* flagellar motor that can use both Na⁺ and K⁺ as a coupling ion is converted by a single mutation to use only Na⁺. *PLoS One* **7**, e46248
- Catterall, W. A., Cest le, S., Yarov-Yarovoy, V., Yu, F. H., Konoki, K., and Scheuer, T. (2007) Voltage-gated ion channels and gating modifier toxins. *Toxicol.* **49**, 124–141
- Bosmans, F., and Swartz, K. J. (2010) Targeting voltage sensors in sodium channels with spider toxins. *Trends Pharmacol. Sci.* **31**, 175–182
- Bosmans, F., Martin-Eauclaire, M. F., and Swartz, K. J. (2008) Deconstructing voltage sensor function and pharmacology in sodium channels. *Nature* **456**, 202–208
- Swartz, K. J. (2007) Tarantula toxins interacting with voltage sensors in potassium channels. *Toxicol.* **49**, 213–230
- Wang, J., Yarov-Yarovoy, V., Kahn, R., Gordon, D., Gurevitz, M., Scheuer, T., and Catterall, W. A. (2011) Mapping the receptor site for alpha-scorpion toxins on a Na⁺ channel voltage sensor [published correction in *Proc. Natl. Acad. Sci. USA* (2014) 111, 3645]. *Proc. Natl. Acad. Sci. USA* **108**, 15426–15431
- Cest le, S., Qu, Y., Rogers, J. C., Rochat, H., Scheuer, T., and Catterall, W. A. (1998) Voltage sensor-trapping: enhanced activation of sodium

- channels by beta-scorpion toxin bound to the S3-S4 loop in domain II. *Neuron* **21**, 919–931
22. Bagnéris, C., DeCaen, P. G., Naylor, C. E., Pryde, D. C., Nobeli, I., Clapham, D. E., and Wallace, B. A. (2014) Prokaryotic NavMs channel as a structural and functional model for eukaryotic sodium channel antagonism. *Proc. Natl. Acad. Sci. USA*
 23. Tang, C., Zhou, X., Zhang, Y., Xiao, Z., Hu, Z., Zhang, C., Huang, Y., Chen, B., Liu, Z., and Liang, S. (2015) Synergetic action of domain II and IV underlies persistent current generation in Nav1.3 as revealed by a tarantula toxin. *Sci. Rep.* **5**, 9241
 24. Xiao, Y., Bingham, J. P., Zhu, W., Moczydlowski, E., Liang, S., and Cummins, T. R. (2008) Tarantula huwentoxin-IV inhibits neuronal sodium channels by binding to receptor site 4 and trapping the domain II voltage sensor in the closed configuration. *J. Biol. Chem.* **283**, 27300–27313
 25. Wang, C., Bradley, P., and Baker, D. (2007) Protein-protein docking with backbone flexibility. *J. Mol. Biol.* **373**, 503–519
 26. Mandell, D. J., Coutsiadis, E. A., and Kortemme, T. (2009) Sub-angstrom accuracy in protein loop reconstruction by robotics-inspired conformational sampling. *Nat. Methods* **6**, 551–552
 27. Yarov-Yarovoy, V., DeCaen, P. G., Westebroek, R. E., Pan, C. Y., Scheuer, T., Baker, D., and Catterall, W. A. (2012) Structural basis for gating charge movement in the voltage sensor of a sodium channel. *Proc. Natl. Acad. Sci. USA* **109**, E93–E102
 28. Yarov-Yarovoy, V., Schonbrun, J., and Baker, D. (2006) Multipass membrane protein structure prediction using Rosetta. *Proteins* **62**, 1010–1025
 29. Barth, P., Schonbrun, J., and Baker, D. (2007) Toward high-resolution prediction and design of transmembrane helical protein structures [published correction in *Proc. Natl. Acad. Sci. USA* (2007) 104, 20635]. *Proc. Natl. Acad. Sci. USA* **104**, 15682–15687
 30. Tao, X., Lee, A., Limapichat, W., Dougherty, D. A., and MacKinnon, R. (2010) A gating charge transfer center in voltage sensors. *Science* **328**, 67–73
 31. Conway, P., Tyka, M. D., DiMaio, F., Konerding, D. E., and Baker, D. (2014) Relaxation of backbone bond geometry improves protein energy landscape modeling. *Protein Sci.* **23**, 47–55
 32. Qu, Y., Liang, S., Ding, J., Liu, X., Zhang, R., and Gu, X. (1997) Proton nuclear magnetic resonance studies on huwentoxin-I from the venom of the spider *Selenocosmia huwena*: 2. Three-dimensional structure in solution. *J. Protein Chem.* **16**, 565–574
 33. Gray, J. J., Moughon, S., Wang, C., Schueler-Furman, O., Kuhlman, B., Rohl, C. A., and Baker, D. (2003) Protein-protein docking with simultaneous optimization of rigid-body displacement and side-chain conformations. *J. Mol. Biol.* **331**, 281–299
 34. Sheets, M. F., and Hanck, D. A. (2003) Molecular action of lidocaine on the voltage sensors of sodium channels. *J. Gen. Physiol.* **121**, 163–175
 35. Lee, S., Goodchild, S. J., and Ahern, C. A. (2012) Local anesthetic inhibition of a bacterial sodium channel. *J. Gen. Physiol.* **139**, 507–516
 36. Lee, S., Goodchild, S. J., and Ahern, C. A. (2012) Molecular and functional determinants of local anesthetic inhibition of NaChBac. *Channels (Austin)* **6**, 403–406
 37. Bagnéris, C., DeCaen, P. G., Naylor, C. E., Pryde, D. C., Nobeli, I., Clapham, D. E., and Wallace, B. A. (2014) Prokaryotic NavMs channel as a structural and functional model for eukaryotic sodium channel antagonism. *Proc. Natl. Acad. Sci. USA* **111**, 8428–8433
 38. Phillips, L. R., Milescu, M., Li-Smerin, Y., Mindell, J. A., Kim, J. I., and Swartz, K. J. (2005) Voltage-sensor activation with a tarantula toxin as cargo. *Nature* **436**, 857–860
 39. Lee, H. C., Wang, J. M., and Swartz, K. J. (2003) Interaction between extracellular Hanatoxin and the resting conformation of the voltage-sensor paddle in Kv channels. *Neuron* **40**, 527–536
 40. Li-Smerin, Y., and Swartz, K. J. (2000) Localization and molecular determinants of the Hanatoxin receptors on the voltage-sensing domains of a K(+) channel. *J. Gen. Physiol.* **115**, 673–684
 41. Stevens, M., Peigneur, S., and Tytgat, J. (2011) Neurotoxins and their binding areas on voltage-gated sodium channels. *Front. Pharmacol.* **2**, 71
 42. Martin, L. J., and Corry, B. (2014) Locating the route of entry and binding sites of benzocaine and phenytoin in a bacterial voltage gated sodium channel. *PLoS Comput. Biol.* **10**, e1003688
 43. Raju, S. G., Barber, A. F., LeBard, D. N., Klein, M. L., and Carnevale, V. (2013) Exploring volatile general anesthetic binding to a closed membrane-bound bacterial voltage-gated sodium channel via computation. *PLoS Comput. Biol.* **9**, e1003090
 44. Tao, H., Wu, Y., Deng, M., He, J., Wang, M., Xiao, Y., and Liang, S. (2013) Molecular determinants for the tarantula toxin jingzhaotoxin-I interacting with potassium channel Kv2.1. *Toxicol.* **63**, 129–136
 45. Xiao, Y., Tang, J., Hu, W., Xie, J., Maertens, C., Tytgat, J., and Liang, S. (2005) Jingzhaotoxin-I, a novel spider neurotoxin preferentially inhibiting cardiac sodium channel inactivation. *J. Biol. Chem.* **280**, 12069–12076
 46. Chanda, B., and Bezanilla, F. (2002) Tracking voltage-dependent conformational changes in skeletal muscle sodium channel during activation. *J. Gen. Physiol.* **120**, 629–645
 47. Campos, F. V., Chanda, B., Beirão, P. S., and Bezanilla, F. (2008) Alpha-scorpion toxin impairs a conformational change that leads to fast inactivation of muscle sodium channels. *J. Gen. Physiol.* **132**, 251–263
 48. Capes, D. L., Arcisio-Miranda, M., Jarecki, B. W., French, R. J., and Chanda, B. (2012) Gating transitions in the selectivity filter region of a sodium channel are coupled to the domain IV voltage sensor. *Proc. Natl. Acad. Sci. USA* **109**, 2648–2653
 49. Capes, D. L., Goldschen-Ohm, M. P., Arcisio-Miranda, M., Bezanilla, F., and Chanda, B. (2013) Domain IV voltage-sensor movement is both sufficient and rate limiting for fast inactivation in sodium channels. *J. Gen. Physiol.* **142**, 101–112
 50. Bacongus, I., and Gouaux, E. (2012) Structural plasticity and dynamic selectivity of acid-sensing ion channel-spider toxin complexes. *Nature* **489**, 400–405
 51. Bacongus, I., Bohlen, C. J., Goehring, A., Julius, D., and Gouaux, E. (2014) X-ray structure of acid-sensing ion channel I-snake toxin complex reveals open state of a Na(+)-selective channel. *Cell* **156**, 717–729
 52. Cao, E., Liao, M., Cheng, Y., and Julius, D. (2013) TRPV1 structures in distinct conformations reveal activation mechanisms. *Nature* **504**, 113–118
 53. Scheuer, T. (2014) Bacterial sodium channels: models for eukaryotic sodium and calcium channels. *Handb. Exp. Pharmacol.* **221**, 269–291
 54. Naylor, C. E., Bagnéris, C., DeCaen, P. G., Sula, A., Scaglione, A., Clapham, D. E., and Wallace, B. A. (2016) Molecular basis of ion permeability in a voltage-gated sodium channel. *EMBO J.* **35**, 820–830
 55. Zhou, Y., Morais-Cabral, J. H., Kaufman, A., and MacKinnon, R. (2001) Chemistry of ion coordination and hydration revealed by a K+ channel-Fab complex at 2.0 Å resolution. *Nature* **414**, 43–48
 56. Zhou, Y., and MacKinnon, R. (2003) The occupancy of ions in the K+ selectivity filter: charge balance and coupling of ion binding to a protein conformational change underlie high conduction rates. *J. Mol. Biol.* **333**, 965–975
 57. DeCaen, P. G., Yarov-Yarovoy, V., Zhao, Y., Scheuer, T., and Catterall, W. A. (2008) Disulfide locking a sodium channel voltage sensor reveals ion pair formation during activation. *Proc. Natl. Acad. Sci. USA* **105**, 15142–15147
 58. DeCaen, P. G., Yarov-Yarovoy, V., Sharp, E. M., Scheuer, T., and Catterall, W. A. (2009) Sequential formation of ion pairs during activation of a sodium channel voltage sensor. *Proc. Natl. Acad. Sci. USA* **106**, 22498–22503
 59. DeCaen, P. G., Yarov-Yarovoy, V., Scheuer, T., and Catterall, W. A. (2011) Gating charge interactions with the S1 segment during activation of a Na+ channel voltage sensor. *Proc. Natl. Acad. Sci. USA* **108**, 18825–18830
 60. Catterall, W. A. (2014) Structure and function of voltage-gated sodium channels at atomic resolution. *Exp. Physiol.* **99**, 35–51

Received for publication September 1, 2016.

Accepted for publication March 27, 2017.

A novel tarantula toxin stabilizes the deactivated voltage sensor of bacterial sodium channel

Cheng Tang, Xi Zhou, Phuong Tran Nguyen, et al.

FASEB J published online April 11, 2017

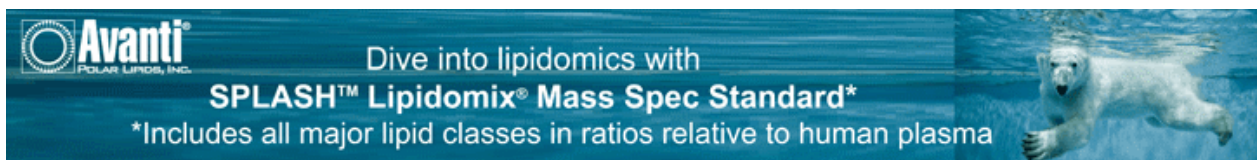
Access the most recent version at doi:[10.1096/fj.201600882R](https://doi.org/10.1096/fj.201600882R)

Supplemental Material <http://www.fasebj.org/content/suppl/2017/04/11/fj.201600882R.DC1>

Subscriptions Information about subscribing to *The FASEB Journal* is online at <http://www.faseb.org/The-FASEB-Journal/Librarian-s-Resources.aspx>

Permissions Submit copyright permission requests at: <http://www.fasebj.org/site/misc/copyright.xhtml>

Email Alerts Receive free email alerts when new an article cites this article - sign up at <http://www.fasebj.org/cgi/alerts>



Avanti
POLAR LIPIDS, INC.

Dive into lipidomics with
SPLASH™ Lipidomix® Mass Spec Standard*

*Includes all major lipid classes in ratios relative to human plasma

SUPPLEMENTAL MATERIAL

A novel tarantula toxin stabilizes the deactivated voltage sensor of bacterial sodium channel

Cheng Tang^{a,1}, Xi Zhou^{a,1}, Phuong Tran Nguyen^c, Yunxiao Zhang^a, Zhaotun Hu^a, Changxin Zhang^a, Vladimir Yarov-Yarovoy^{c,2}, Paul G. DeCaen^{b,2}, Songping Liang^{a,2} and Zhonghua Liu^{a,2}

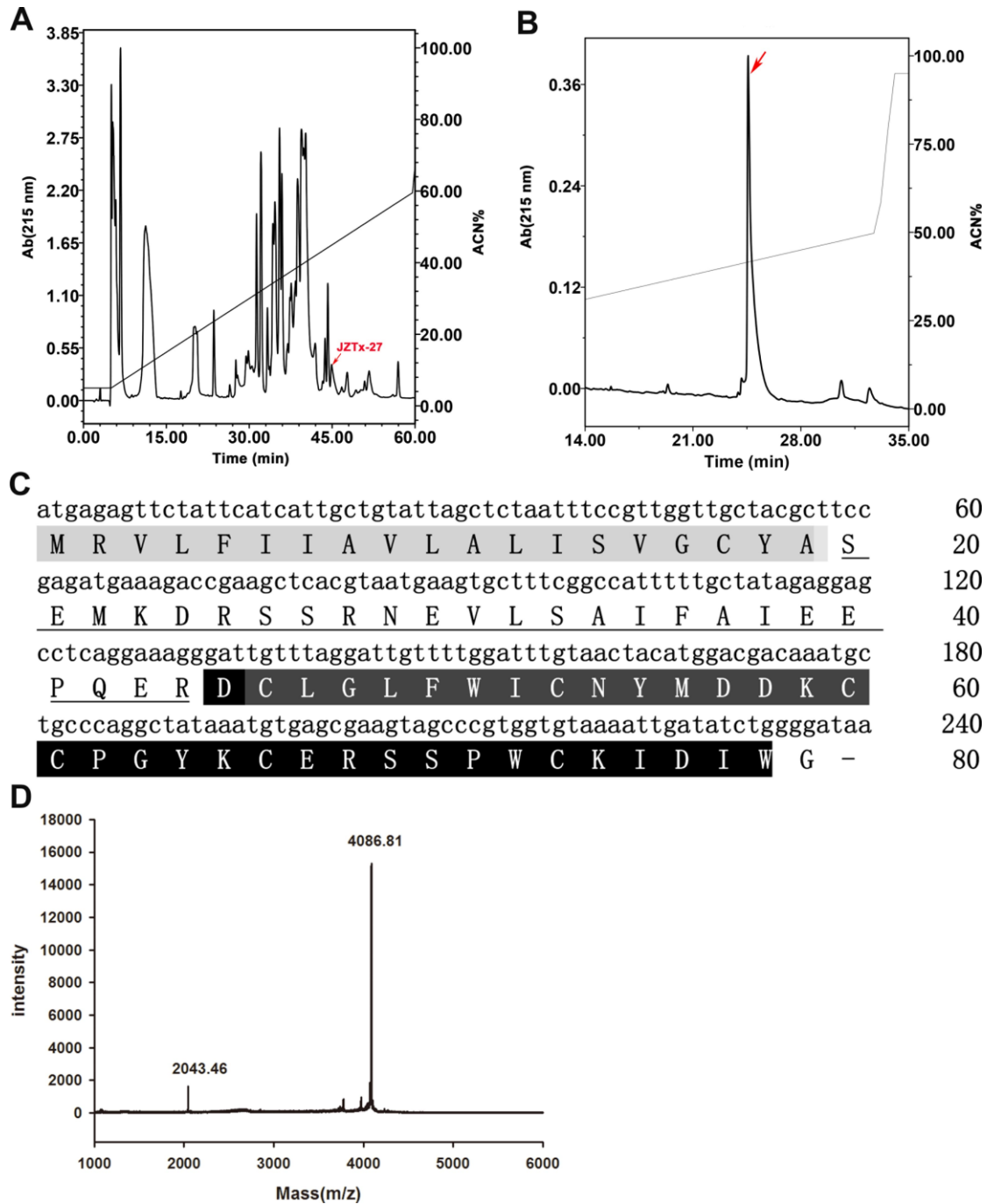
^aThe National & Local Joint Engineering Laboratory of Animal Peptide Drug Development, College of Life Sciences, Hunan Normal University, Changsha 410081, Hunan, China;

^bDepartment of Pharmacology, Feinberg School of Medicine, Northwestern University, Chicago IL, 60611, USA;

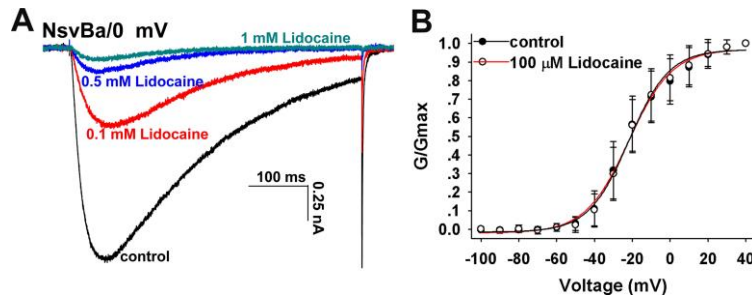
^cDepartment of Physiology and Membrane Biology, University of California Davis, Davis, CA 95616, USA;

¹C.T., X.Z. contributed equally to this work.

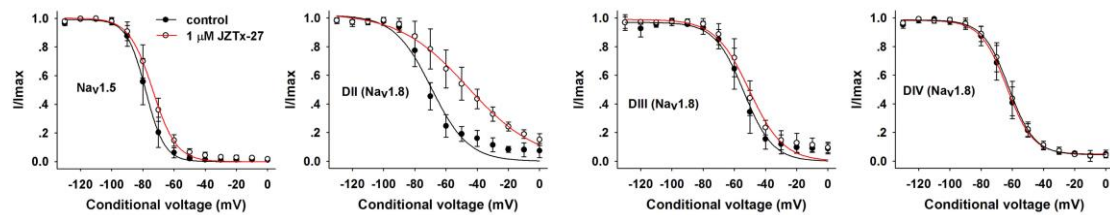
²To whom correspondence may be addressed. E-mail: Vladimir Yarov-Yarovoy, yarovoy@ucdavis.edu; Paul G. DeCaen, Paul.DeCaen@northwestern.edu; Songping Liang, liangsp@hunnu.edu.cn; Zhonghua Liu, liuzh@hunnu.edu.cn



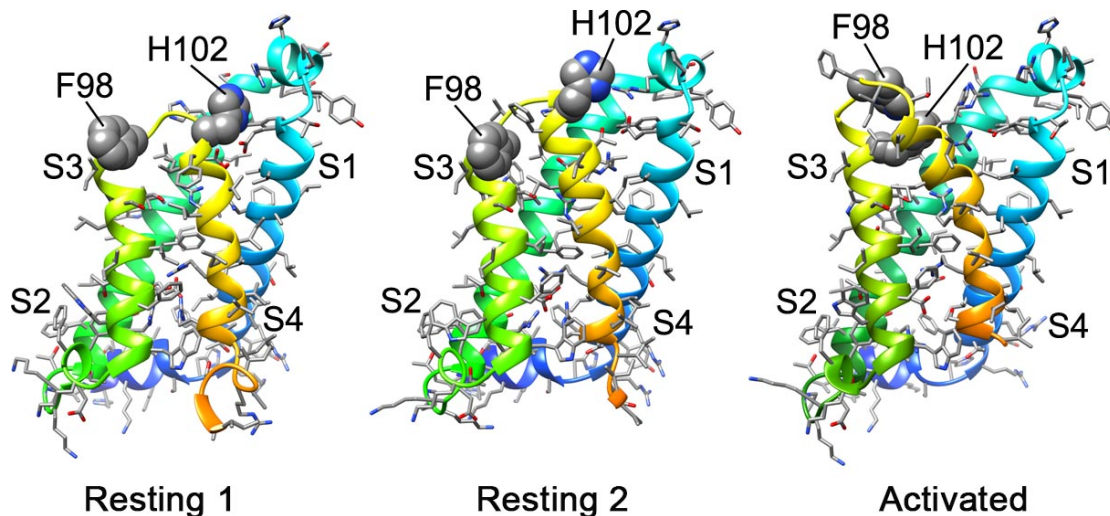
Supplemental Fig.S1. (A) RP-HPLC profile of the venom from *Chilobrachys jingzhao*. Red arrow indicates the fraction containing JZTx-27. (B) The peak containing JZTx-27 in Supplemental Fig.S1A was further purified by analytical C₁₈ RP-HPLC. Red arrow indicates the purified JZTx-27. (C) The molecular weight of JZTx-27 was determined as 4086.81Da (M+H⁺) by MALDI-TOF MS.(D) cDNA and amino acid sequence of JZTx-27. The mature sequence (shaded in black) was also determined by Edman degradation; the signal peptide is shown in gray, and the propeptide is underlined.



Supplemental Fig.S2. (A), Representative traces showing lidocaine blocks NsvBa current dose-dependently. (B), Lidocaine treatment did not alter the steady-state activation of NsvBa.



Supplemental Fig.S3. Steady-state inactivation curves of Nav_v1.5, DII(Nav_v1.8), DIII(Nav_v1.8) and DIV(Nav_v1.8) chimeric channels before and after application of 1 μM JZTX-27. Toxin dramatically modified the voltage dependence of inactivation of DII(Nav_v1.8) but not others by shifting the V_h from -72.1 ± 3.0 mV to -53.1 ± 11.4 mV ($p = 0.00685$) and increasing the K_h from -7.4 ± 2.5 mV to -14.9 ± 1.6 mV ($p = 0.00044$).



Supplemental Fig.S4. Transmembrane view of structural models of NsvBa in resting and activated states. Transmembrane segments S1 through S4 are colored by rainbow

color scheme from blue (S1) to orange (S4) and labeled. Sidechains of key residues for JZTx-27 binding are shown in space-filling representation and labeled. Sidechains of all other residues are shown in stick representation.

Supplemental table.S1. The voltage evoking the maximum peak current of each mutant/chimeric channel. Data was presented as MEAN \pm SD (n = 4 - 12).

| Mutant | V_{peak} | Mutant | V_{peak} |
|------------------------------|-------------------------|--------------------------|-------------------------|
| Ns _v Ba Y40A/P41A | -32.5 \pm 22.2 | Ns _v Ba F98A | -44 \pm 8.9 |
| Ns _v Ba L43A | -32.5 \pm 5.0 | Ns _v Ba F98P | 8.3 \pm 4.1 |
| Ns _v Ba R44A/H45A | -46.0 \pm 11.4 | Ns _v Ba V99A | 2.9 \pm 7.6 |
| Ns _v Ba E46A/Y47A | -34.0 \pm 5.5 | Ns _v Ba H102Q | -58.0 \pm 8.4 |
| Ns _v Ba S94A | -30.0 \pm 10.0 | Ns _v Ba F103G | -48.3 \pm 11.7 |
| Ns _v Ba S95A | 5.0 \pm 10.5 | Ns _v Ba I104L | -17.5 \pm 5.0 |
| Ns _v Ba H96A | 4.0 \pm 5.5 | wt Ns _v Ba | -3.4 \pm 6.2 |
| Ns _v Ba I97A | -35.0 \pm 13.8 | Chimera 2 | -20.0 \pm 11.0 |

V_{peak}: the voltage evoking the maximum peak current